Atomic hydrogen induced defect kinetics in amorphous silicon

F. J. J. Peeters[1,2], J. Zheng[3], I. M. P. Aarts[2], A. C. R. Pipino[2], W. M. M. Kessels[2], M. C. M. van de Sanden[1,2]

[1]DIFFER - Dutch Institute for Fundamental Energy Research, De Zaale 20, 5612 AJ Eindhoven, the Netherlands

[2]Eindhoven University of Technology, Department of Applied Physics, PO Box 513, NL-5600 MB Eindhoven, The Netherlands

[3]Beijing National Laboratory for Molecular Sciences (BNLMS), College of Chemistry and Molecular Engineering, Peking University, 5 Yiheyuan Road, Beijing, 100871, P.R. China.

Abstract:

Near-IR Evanescent-Wave Cavity Ring-Down Spectroscopy (EW-CRDS) has been applied to study the defect evolution in an a-Si:H thin film subjected to a directed beam of atomic H with a flux of (0.4-2) x 10^{14} cm^{-2}s^{-1}. To this end a 42 ± 2 nm a-Si:H film was grown on the Total Internal Reflection (TIR) surface of a folded miniature optical resonator by Hot-Wire Chemical Vapor Deposition (HW-CVD). A fully reversible defect creation process is observed, with a non-linear dependence on H flux, with a time resolution of 33 ms and a relative sensitivity of 10^{-7}. Through the use of polarizing optics the CRDS signal was split into *s*- and *p*-polarized components, which, combined with *E*-

field calculations, provides depth sensitivity. Extensive kinetic modeling of the observed process is used to determine rate constants for the hydrogen-material interactions and defect formation in a-Si:H, as well as revealing a high diffusion coefficient for atomic H on the order of 10^{-11} cm^{2}s^{-1}. A novel reaction pathway is proposed whereby H inserted into weak Si-Si bonds recombines with mobile H, resulting in a limited penetration depth for atomic H from the gas-phase on the order of 10 - 15 nm.

I. INTRODUCTION

This work demonstrates the use of a monolithic optical resonator to detect defect states in thin films during exposure to a directed atomic beam, as well as introducing a physical model describing the results. The thin film chosen is hydrogenated amorphous silicon (a-Si:H) grown by Hot-Wire Chemical Vapor Deposition (HW-CVD). Hydrogenated amorphous silicon has received considerable attention in the field of plasma processing due to its ubiquitous uses in electronic and optoelectronic devices. The interaction of atomic hydrogen with a-Si:H plays a crucial role in both the film growth [1] and the reversible light-induced degradation known as the Staebler-Wronski (SW) effect [2]. During growth, hydrogen is required to minimize the dangling bond defect density and is known to induce disorder-to-order structural transitions in the material [3-7]. In the SW effect, redistributions of small amounts of hydrogen liberated by photons into meta-stable configurations are commonly attributed as the source of electronic degradation [8-11]. However, the exact mechanism behind the SW effect is still unknown [12-14].

Over the years, numerous surface science studies have been devoted to crystalline silicon (c-Si), with its well-defined reconstructed surfaces [15-19]. Initially, it was found that the abstraction and adsorption reactions by atomic H followed Eley-Rideal (ER) or hot precursor (HP) reaction schemes [19], respectively. However Küppers and co-workers showed that H can also be abstracted through indirect pathways [16], while Flowers *et al.* [17] and later Inanaga *et al.* [20] showed a quasi equilibrium model of surface species should be used to explain the uptake kinetics more precisely. In principle, the experiments on c-Si can provide qualitative understanding of the kinetics of hydrogen

interacting with a-Si:H. However, the amorphous nature of the Si thin films complicates the interpretation of reaction mechanisms considerably. Several *in situ* experiments have been carried out to establish the interaction of atomic H with a-Si:H, including experiments based on nuclear magnetic resonance [21], hydrogen effusion [22], (spectroscopic) ellipsometry [23-25] and IR absorption spectroscopy [26,27]. Although, important insight into the interaction of H with a-Si:H was obtained, detailed insight into the reaction kinetics of H and its relation with defect density was not obtained. Because most diagnostics used are based on the detection of hydrogen species, the interpretation of these kinds of experiments can be complicated due to the fact that a-Si:H contains a large amount of bulk hydrogen, making it difficult to distinguish the interaction of atomic H with a-Si:H. To obtain a full understanding of the interaction of atomic H with a-Si:H, particularly with respect to its role in the creation and passivation of defects, it is beneficial to probe the defect density, preferentially *in situ* and during hydrogen treatment.

Monitoring the defects also allows direct determination of the mobile hydrogen diffusion coefficient, as opposed to the effective diffusion coefficient obtained from SIMS studies on deuterium treated a-Si:H films [23-28]. Such a measurement of the mobile hydrogen diffusion coefficient can set boundaries to certain SW models. Das *et al.* have reported on *in situ* electron spin resonance experiments where a-Si:H films were exposed to a flux of atomic hydrogen in the range of 10^{15} - 10^{17} cm^{2}s^{-1} [34-36]. It was observed that H dosing induces up to $4 \cdot 10^{13}$ cm^{-2} additional sub-surface dangling bonds, dependent on film thickness, but independent of the flux for their conditions, which reversibly decay after the flux is terminated. From the observed penetration depth of

dangling bond formation a high diffusion coefficient ($> 10^{-10}$ cm^{2}s^{-1}) for atomic H in a-Si:H was derived. However, their model to account for dangling bond creation is not validated in detail due to the limited time resolution of the ESR setup of up to 84 s [36].

Silicon dangling bonds can also be detected by near-IR absorption spectroscopy *i.e.*, by probing sub-gap defect states [37-40]. In this paper, we present results of low flux atomic hydrogen dosing ($4 - 20 \cdot 10^{13}$ cm^{2}s^{-1}) of a 42 ± 2 nm a-Si:H film measured by Evanescent Wave CRDS employing a monolithic optical resonator [41]. This technique allows for real-time monitoring of the defect density with a time-resolution of 33 ms and a sensitivity of 10^{-7}, with additional information provided by the *s*- and *p*-polarization anisotropy, as demonstrated by previous experiments on the absolute dangling bond density during growth of *a*-Si:H [38] and the characterization of a quasi-ice monolayer [42]. Another clear advantage of CRDS is that absolute losses can be determined from the ring-down time without the need for calibration.

Our experimental results have sufficient time resolution to apply full kinetic modeling, while the polarization anisotropy allows for depth profiling of the defect density. We will show that additional, self-healing, defects are formed below the surface of the film by low incident atomic H fluxes and propose a kinetic model that accurately describes the kinetics of atomic H in the sub-surface of a-Si:H. We conclude that the penetration depth of atomic H is limited by the formation of H$_2$ at shallow trapping sites in the a-Si:H network, with a high diffusion coefficient of atomic H resulting from the absence of deep trapping sites.

In the following sections, experimental details are presented including the deposition setup, sample preparation, atomic H source, folded resonator and optical

system, as well as spectroscopic ellipsometry and infrared spectroscopy experiments providing data complementary to the EW-CRDS results. Subsequently, the H-dosing data and the extraction of defect density is addressed and a full model presented to account for the EW-CRDS results. In the final sections, the key observations are summarized and H reaction mechanisms in a-Si:H are discussed in light of these results.

II. EXPERIMENTAL

A. UHV setup

A schematic overview of the ultra-high vacuum (UHV) setup is given in Fig. 1a. The UHV setup consists of two stainless steel vacuum chambers (base-pressure $< 10^{-9}$ mbar) that are separated by a flange that holds the folded resonator as a substrate. One chamber contains the sources for deposition and hydrogen dosing, and the other chamber contains a heater (Advanced Ceramics Corporation, Boralectric™ heater model HTR 1002, 1440 W) for substrate heating and provides optical access to the folded resonator. The substrate temperature is actively controlled by a feedback loop using a thermocouple mounted close to the resonator. Deposition of a-Si:H on the Total Internal Reflection (TIR) surface of the resonator takes place by the decomposition of purified silane (SiH_4, Praxair, purity >99.995%, delivered by a mass flow controller) on a hot coiled tungsten filament with a diameter 0.45 mm. A quantified atomic hydrogen flux can be delivered to the substrate by an atomic H source described in more detail below. Both the hot filament and the H source are mounted on linear translators such that the distance between these sources and the substrate can be varied. An automated stainless steel shutter protects the substrate during start up of the sources and provides the opportunity for fast on-and-off switching of the radical fluxes to the TIR surface of the folded resonator.

B. Atomic H-source

The atomic H-source [43,44] consist of a tungsten capillary (length: 6 cm, diameter 1 mm) that is heated by a tungsten filament in which purified H_2 (Praxair, purity >99.999%, delivered by mass flow controller) is dissociated producing an atomic H

7

beam. The spatial H output of the source has been extensively calibrated by mass spectrometry measurements as a function of the polar angle for different capillary temperatures (1800 - 2600 K) and H_2 flows (1.9×10^{-3} - 0.42 sccm) [43,44]. However, an uncertainty in the absolute H flux up to a factor of two cannot be excluded due to uncertainties in the H_2 flow and the exact temperature of the capillary. The H flux onto the substrate can however be changed accurately by varying the distance between the source and the TIR surface of the folded resonator (between 15.4 and 5.4 cm). The H-source acts like a point-source and the H flux therefore shows a $1/r^2$ dependence on the distance r between the substrate and the heated region of the H-source [43,44]. This procedure guarantees an accurate relative H dosing with an absolute accuracy within a factor of two. Initial heating of the tungsten filament resulted in a small <ppm change in the optical loss of the resonator even when protected by the shutter. This effect might be induced by heating effects of the TIR surface or by creation of radical species from the background gasses and etching from the reactor walls. A similar but opposite effect is observed when the source was cooled down. Furthermore, in control experiments it was verified that the heated hydrogen source did not influence the measurements when no hydrogen was supplied to the source.

C. Folded resonator and optical system

A high-finesse ($\mathcal{F}$=63000), high-Q (Q≈10^{10}) ultra-low-loss monolithic folded optical resonator is employed in the H dosing experiments, see Figure 1b [41]. The atomically smooth total-internal reflection (TIR) surface of the resonator forms the

working surface for the experiments after being covered with an a-Si:H thin film [38,45]. The resonator was fabricated from a single, right-triangular monolith of ultra-pure a-SiO$_2$ (< 50 ppb bulk OH by weight; optical loss < 2.3×10^{-6}/cm at 1200 nm), having a 2.0 cm edge dimension and a thickness of 0.5 cm. The two planar, high-reflectivity coated (> 99.998%) surfaces and convex TIR surface (9.0 cm radius of curvature) were chemo-mechanically polished to 0.05 nm root-mean-square surface roughness. The per-pass loss of the resonator was coating-limited, reaching a minimum of 18×10^{-6} at 1205 nm (8299 cm^{-1}), which yielded a base photon storage time (ring-down time) of 5.3 μs. The ring-down time is inversely proportional to the absolute loss and requires no calibration. The area probed by the evanescent field at the apex of the TIR surface is $\pi\sqrt{2}(85 \times 99)$ μm^2 for the fundamental resonator mode at 1200 nm, which is fixed in position by the monolithic design, providing a precisely defined sample region [46].

The resonator was cleaned with high purity methanol after having been exposed to ambient conditions for a protracted time. Subsequently, the folded resonator was mounted in the center of the substrate holder with the total internal reflection (TIR) surface facing the deposition chamber. After basic alignment using a visible laser beam operating at 532 nm of the in- and outgoing laser beams, the resonator was slowly heated by radiation to the deposition temperature of 120 °C.

The idler of an optical parametric oscillator (Quanta-Ray, MOPO 710) pumped by a seeded, tripled Nd:YAG operating at 30 Hz (Quanta-Ray, 230-30) provided laser pulses of 6 ns duration, and a characteristic linewidth of < 10 cm^{-1}. Using optical components as indicated in Figure 1a, the laser pulse was weakly focused onto the planar surface of the folded resonator using a lens to excite a distribution of low-order modes in the resonator.

Fine alignment of the resonator could be realized using only two alignment mirrors positioned outside the UHV setup. A double Fresnel rhomb (Thorlabs, FR600HM) and a Glan-Laser polarizer (Thorlabs, GL-10) are used to adjust the incident laser power and to control the polarization input. Using equal amounts of *s*- and *p*-polarized input light, the orthogonally polarized ring-down transients were separated using another Glan-Laser polarizer (Thorlabs, GL-10) and simultaneously detected by two free-space-coupled, high-speed, 125 MHz, InGaAs photodiode detectors (New Focus, 1811). The average energy per laser pulse needed to obtain a good signal-to-noise ratio was found to be ≈ 0.5 mJ/pulse, well below the damage threshold of the resonator mirror coatings (≈ 3 mJ/pulse). Each individual ring-down time is extracted from the recorded transient using a weighted least-square fit. The statistical properties of the ring-downs can be stored and averaged to acquire higher sensitivity.

D. Spectroscopic ellipsometry and infrared spectroscopy

Additional information on the a-Si:H material properties and the influence of H dosing were obtained by in situ spectroscopic ellipsometry (SE) and in situ attenuated total reflection (ATR) infrared spectroscopy experiments [47]. The measurement took place under identical conditions in a separate experiment using GaAs ATR crystals (Harrick) with native oxide. From the SE measurements (photon energy range: 1.5-5.0 eV) the film thickness and the optical material properties of the a-Si:H thin film were obtained. The ATR infrared spectroscopy measurements (wavenumber range: 800-7000 cm^{-1}, resolution 4 cm^{-1}) gave information on the bulk and surface hydride composition for

the as-deposited films while also the influence of atomic H on the (surface) hydride composition was studied.

E. a-Si:H sample preparation

A 42 ± 2 nm *a*-Si:H film was deposited on the TIR surface by thermal decomposition of SiH_4 on a hot tungsten filament (~ 2050 °C) at a pressure of $4 \cdot 10^{-3}$ mbar (prior to HW ignition). The filament was located 6.8 cm from the resonator surface which was heated to 120 °C, leading to a growth rate of ~ 2.5 nm/min under conditions where SiH_3 is considered to be the dominant growth precursor [48-50]. Separate depositions studied using infrared spectroscopy reveal a dominant contribution of the lower stretching mode (LSM) and a 70% smaller contribution of the higher stretching mode (HSM) with a total hydrogen content of ~ 13 at%, pointing to a dominance of (di-)vacancies over nanosized voids in the material. This is supported further by spectroscopic ellipsometry measurements, revealing a refractive index of 4.3 (3.6) at a wavelength of 600 (1200) nm, indicative of dense *a*-Si:H with a minimum contribution of nanosized voids [27,51].

H dosing was carried out by cracking a 0.1 sccm H_2 flow in the atomic H source heated to a temperature of ~ 1850 K by a filament current of 9 A. The largest H flux ($2 \cdot 10^{14}$ cm^{-2}s^{-1}) was obtained for a distance of 5.4 cm to the resonator surface while the smallest H flux ($0.42 \cdot 10^{14}$ cm^{-2}s^{-1}) was obtained at the maximum separation between source and resonator of 15.4 cm. Spectroscopic ellipsometry measurements indicate that under these conditions a negligible amount of *a*-Si:H is etched ($<10^{-3}$ nm/s at the highest flux). An automated stainless steel shutter protects the substrate during startup of the H

source and provides the opportunity for fast on-and-off switching of the atomic H flux to the resonator surface.

Both EW-CRDS and ATR infrared spectroscopy measurements reveal that the *a*-Si:H film undergoes structural changes within the first few minutes after deposition and that atomic H dosing initially removes Si-H$_2$ and Si-H$_3$ groups at the surface while inducing minor changes in the bonding configuration sub-surface. Because the focus of this work is on studying defect kinetics as a function of atomic H flux, a fully reversible response to the H flux is preferred. For this reason the as-grown film was pre-treated with a $2 \cdot 10^{14}$ cm^{-2}s^{-1} flux of atomic H for 2 h in steps of approximately 30 s (totaling ~ 1000 monolayers of H), ensuring that the film does not undergo structural changes during the subsequent H dosing series. During H pre-treatment of the film only minor variations (1-3 ppm for *s*-polarization) in the background optical loss of the film were observed.

III. RESULTS AND DISCUSSION

A. Controlled H-dosing experiments

The EW-CRDS signal was measured continuously with the H flux being varied from $2 \cdot 10^{14}$ cm^{-2}s^{-1} to $0.42 \cdot 10^{14}$ cm^{-2}s^{-1} in 11 steps of 30 s, see Figure 2. The sub-gap absorption is seen to increase rapidly up to double the original loss level when an H flux is incident on the film surface, but returns gradually to the original loss level when the flux is turned off.

The initial rate of increase of the loss upon H dosing (referred to as the creation rate), was determined from exponential fitting of the data and extrapolating to the time the flux was turned on. This shows an almost linear dependence of the initial rate on flux, see Figure 3a. Moreover, subsequent linear fits of this data show an *s/p* polarization ratio of 2.8 ± 0.1. Because of the 30 Hz sampling rate of the optical system, this polarization ratio is reached at least 33 ms after the flux is turned on and may not represent the exact initial *s/p* ratio upon H irradiation. The steady-state is attained within 15 s after the flux is turned on and shows a non-linear dependence on flux as well as a distinct polarization ratio of 3.7 ± 0.2, as can be seen in Figure 3b. With increasing flux, the defect absorption also appears to approach a saturation level for both polarization directions. The *p*-polarized optical loss reaches the steady-state faster than the *s*-polarized loss as shown in Figure 4, though the decay after the flux is turned off occurs at roughly the same rate for both polarization directions. The inset of Figure 4 shows the inverse of the decay for s-polarization, revealing a distinct hyperbolic dependence for the decay process. This hyperbolic decay over time clearly indicates that a second order process dominates the healing of defects, which is a leading aspect of the kinetic model presented below.

13

B. Model

A first experimental observation is that repeated H dosing does not affect the background optical loss of the film. This confirms that no structural changes of the film are taking place (such as etching or significant additional hydrogen incorporation), and that the pre-existing defect density, both on the surface and in the bulk, remains unaffected by repeated small H doses.

The optical loss $\Gamma(t)$ can be directly related to the defect density in the thin film by the expression

$$\Gamma(t) = \int_0^h \sigma_{defect} N_{defect}(z,t) I(z) dz \qquad (1)$$

where $I(z)$ is the electric field intensity in the film during ring-down, $N_{defect}(z,t)$ the distribution of defects in the film, σ_{defect} the optical absorption cross-section at the wavelength under consideration and h the thickness of the film. The electric field intensity as a function of depth can be calculated using Fresnel reflection-transmission coefficients [52], while we assume the absorption cross-section is independent of depth with a value of $\sim 10^{-16}$ cm^2 [53].

The E-field intensity depends critically on the polarization direction; see Figure 5 for the calculated E-fields in a 42 nm film. Assuming an isotropic orientation of defects, the s/p polarization ratio can be employed to determine the depth up to which defects are induced by the atomic H flux. An s/p ratio of 2.8 ± 0.1 was determined for the initial creation rate after the flux is turned on (Figure 3a), which for a 42 nm thick film

corresponds with the ratio of E-field intensities just below the surface of the a-Si:H film. Furthermore, the increased s/p ratio of 3.7 ± 0.2 observed in the steady-state can be accounted for by an exponentially decaying defect distribution with a characteristic 1/10 penetration depth of ~ 15 nm. Considering that the penetration depth is significantly lower than the film thickness, it is tentatively assumed that thicker films would show a similar response to H dosing. The s/p ratio and this penetration depth are roughly the same for all fluxes, while the absolute absorption is non-linear in flux (Figure 3b). The non-linearity is therefore not a result of a variable penetration depth, but can be explained by the H kinetics in a thin a-Si:H film. It is of importance to note that the s/p ratios observed in the data do not correspond to fields on the vacuum side of the film surface, where an s/p ratio of 0.13 is expected. This implies that surface defects have (1) a low absorption cross-section at 1200 nm, or (2) are only subject to the E-field intensity just within the film, or (3) are subject to a fast H-induced passivation mechanism (*e.g.* a Kisliuk type of adsorption-abstraction equilibrium [54]). The background loss observed in between H dosing cycles, meanwhile, is consistent with a bulk defect density of $2.4 \cdot 10^{17}$ cm^{-3}.

Using a kinetic model, we will show that our data can be fully accounted for by assuming that all H-induced defect creation observed in our data occurs sub-surface. The increase in sub-surface defect absorption during H dosing implies that atomic H residing in the a-Si:H network can give rise to additional defect states in the gap. This suggests that mobile atomic H penetrating into the bulk of the film encounters locations in the network where it is immobilized and causes the formation of a defect. A likely candidate for this process is the (reversible) insertion of atomic H in strained Si-Si bonds [55-59],

leading to a short-lived configuration of a single bonded H atom (Si-H) with a corresponding dangling bond defect (Si•):

$$Si - Si + H \leftrightarrow Si\bullet\text{--}H\text{-}Si \tag{2}$$
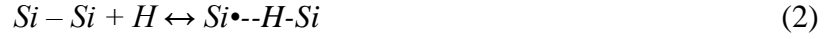
Note that Reaction (2) occurs in both directions, with both insertion of H and desorption of H an essential part of the kinetic model. A short-lived defect naturally explains the complete reversibility observed in the data. The dangling bonds accompanied by neighboring Si-H bonds are designated as *defect complexes* to differentiate them from pre-existing dangling bonds. Because of the limited penetration depth observed for defect creation and the apparent saturation of defects with increasing flux, combined with the t^{-1} dependence of the optical loss decay after the flux is terminated (see the inset of Figure 4), the induced defect density must undergo a quadratic loss process. We propose the recombination of a defect complex with a mobile H atom:

$$Si\bullet\text{--}H\text{-}Si + H \rightarrow Si - Si + H_2 \tag{3}$$

The molecular hydrogen formed in this process is considered inert in terms of defect creation and is expected to diffuse out of the film. It is, however, equally possible that molecular hydrogen remains trapped in voids and divacancies within the *a*-Si:H film [45,60,61].

The abstraction of pre-existing bonded H in the bulk *a*-Si:H and the subsequent passivation of the resulting dangling bonds are not included in the kinetic model, as was

16

done by Das *et al.* in the analysis of their ESR data [35]. Although an abstraction-passivation mechanism will also lead to a limited penetration depth for defect creation, the main objection against this reaction scheme is that defects created through abstraction are not self-healing and therefore cannot account for the complete reversibility observed in the data. As we will show, Reactions (2) and (3) are sufficient reaction pathways to account for our data.

The kinetic equation for H-induced defect complexes can be written as

$$\frac{\partial N_c(z,t)}{\partial t} = k_{ins} N_S N_H(z,t) - k_{rec} N_c(z,t) N_H(z,t) - \frac{N_c(z,t)}{\tau},\tag{4}$$

where $N_c(z,t)$ is the density of inserted H complexes, $N_H(z,t)$ the density of mobile atomic H, k_{ins} is the rate constant for creation of defect complexes, N_S the density of strained Si-Si bonds, τ the self-healing life time of the complex and k_{rec} the recombination rate constant for the process in Equation (3). We assume that the density of available insertion sites N_S is sufficiently high to be considered a local constant. Atomic H diffuses through the film, leading to a corresponding kinetic equation for N_H:

$$\frac{\partial N_H(z,t)}{\partial t} = D_H \frac{\partial^2 N_H(z,t)}{\partial z^2} - k_{ins} N_S N_H(z,t) - k_{rec} N_c(z,t) N_H(z,t) + \frac{N_c(z,t)}{\tau}\tag{5}$$

with D_H the diffusion coefficient for mobile atomic H in the film. We assume that D_H is constant over the flux range considered.

The following boundary condition for the mobile H density N_H at the surface of the film is implemented:

$$-D_H \left. \frac{\partial N_H(z,t)}{\partial z} \right|_{z \downarrow 0} = f\Phi_H . \tag{6}$$

The boundary condition at the a-Si:H–resonator interface is a simple Neumann boundary condition, as atomic H is not expected to penetrate into the fused silica folded cavity:

$$-D_H \left. \frac{\partial N_H(z,t)}{\partial z} \right|_{z \uparrow h} = 0 \tag{7}$$

The parameter Φ_H is the hydrogen flux incident at the surface and f the effective fraction of this flux entering the film. Note that this boundary condition bypasses any interactions of H with the surface of the film by only considering the effective fraction of the flux contributing to sub-surface defect creation. The concentration of mobile H just below the surface ($N_H|_{z \downarrow 0}$) approaches steady-state within $(k_{ins}N_S)^{-1} \approx 10^{-3}$ s (see below) after the H flux is turned on, which is much faster than the experimental time resolution of 33 ms. The experiment is therefore not sensitive to the initial kinetics of atomic H impinging on the surface and the atomic H present just below the surface of the film. In other words, the fraction f is an effective value related to the consumption of H in recombination processes in the sub-surface region. The following relation, derived from Equations (4-7), holds for all fluxes Φ_H:

$$\frac{1}{2}f\Phi_H = \int_0^d k_{rec}N_c(z,t)N_H(z,t)dz\Bigg|_{t\to\infty} \tag{8}$$

The fraction f is therefore a measure of the thickness integrated sub-surface recombination rate.

By fitting the model described by Equations (4-7) to the EW-CRDS data via Equation (1) the parameters $k_{ins}N_S$, k_{rec}, τ, D_H and f are determined. In the fitting procedure the total Mean Squared Error (MSE) over time is simultaneously minimized for the H induced loss of the two highest and the two lowest fluxes, leading to convergence of all five parameters. The lowest total MSE was obtained for a film thickness of 41 nm, though varying the film thickness by a few nanometers has only a small effect on the E-field intensities and, hence, on the quality of the fit.

We can account for all the features in the data, including the polarization anisotropy, steady-state loss and the initial creation/healing rate as a function of H flux using $f = (5.5 \pm 0.1) \cdot 10^{-3}$, $\tau = 0.25 \pm 0.01$ s, $k_{ins}N_S = 800_{-500}^{+100}$ s^{-1}, $k_{rec} = 10_{-6}^{+1} \cdot 10^{-16}$ cm^{3}s^{-1} and $D_H = 3.6_{-2.3}^{+0.5} \cdot 10^{-11}$ cm^{2}s^{-1}, see Figure 6. All values are determined within a 95 % confidence interval, with the errors in $k_{ins}N_S$, k_{rec} and D_H being interdependent. The model predicts a near-surface steady-state density of induced defects $N_c = 4 \cdot 10^{17}$ cm^{-3} and a density of mobile atomic H as low as $N_H = 6 \cdot 10^{15}$ cm^{-3} at an H flux of $2 \cdot 10^{14}$ cm^{2}s^{-1}, see Figure 7 for the calculated H induced defect and mobile H density profiles as a function of depth. The model predicts a saturation defect density $k_{ins}N_S/k_{rec} = 8 \times 10^{17}$ cm^{-3} at high H flux conditions ($\Phi_H > 10^{16}$ cm^{-2}s^{-1}), consistent with the ESR results of Das et $al.$ (10^{13} cm^{-2} with a penetration depth of 100 nm) [35].

The fact that the p-polarized optical loss reaches the steady-state faster than the s-polarized loss can be attributed to the difference in E-field intensities as a function of depth; the s-polarized loss is more sensitive to the small increases in defect density deeper into the film that occur several seconds after the H flux has been turned on.

C. Model discussion:

1. Surface processes

The EW-CRDS data can be completely accounted for by interactions of H in the sub-surface of the a-Si:H film, using three reaction pathways (insertion, desorption and recombination) without there being a clear contribution of additional defects created at the surface during H dosing. As described above, this could be due to rapid equilibration of the surface defect density with the impinging H flux, well within the 30 ms time resolution of the experiment. In this case, the lack of need to include terms for surface defect creation in the model is self-evident. It can also be argued that no measurable change in the surface defect density from atomic H dosing would be detectable at all at treatment temperatures of 120 °C, even with higher time resolution. First of all, abstraction and passivation of H radicals on the film surface are first-order with respect to the incident flux at these temperatures [17,20], leading to an H coverage (and corresponding defect coverage) which is independent of flux. In this case, a fast passivation mechanism will maintain the surface H coverage at the (over-)saturated level prior to dosing [17,20]. This mechanism is driven either by a large reservoir of physisorbed atomic H at the surface, such as in the hot atom Kisliuk model employed by Widdra *et al.* [19] or by a sub-surface atomic H reservoir [62]. Also, at temperatures below 300 °C the surface is stable [22,63-65], so that no desorption of chemisorbed H will occur after dosing is stopped. It is therefore plausible that the surface defect coverage is not significantly altered when the H flux is turned on, especially considering the large H pre-treatment applied to the film, which will have removed any surface configurations unstable to impinging atomic H. In any event, EW-CRDS measurements over a wider

range of sub-gap photon energies are desirable before drawing any definitive conclusions concerning surface defect kinetics in relation to H dosing.

The effective H flux entering the sub-surface of the film is only a small fraction f = 5.5·10^{-3} of the total atomic H flux incident at the surface. However, the fraction f should not be considered the probability of atomic H to enter the film bulk from the surface, as it also includes the amount of desorption of sub-surface H back to the surface or back into the gas-phase. Our model predicts a reservoir of mobile atomic H just below the surface of the film ($\sim$ 10^8 cm^{-2} in the first monolayer), which may contribute to surface abstraction and passivation processes. The rate at which atomic H is returned to the surface cannot be determined, however, so that no conclusions can be drawn about the significance of this reservoir for surface processes.

2. Defect complex and diffusion

The defect complex observed in our data can be identified as a shallow trapping site for atomic H considering the relatively short lifetime τ of 0.25 s compared to the much longer lifetime of deeply trapped H of around 600 ± 200 days (at 180 °C), as determined by Branz *et al.* [66]. A preliminary analysis of an H dosing temperature series revealed an activation energy of ~ 0.25 eV for H desorption from the defect complex, assuming Arrhenius-type behavior. This activation energy for desorption from the defect complex is comparable to the barrier between shallow trap states and transport states of 0.2 - 0.5 eV determined for c-Si [67,68], a-Si [32] or pm/µc-Si [69,70]. In addition, it is well known that diffusion of hydrogen into a-Si:H from a plasma or other external source is dictated by these shallow trap states [28-33]. We do not expect the defect complex (*i.e.*

strained Si-Si bonds) to be the dominant shallow trapping site in a-Si:H, however, since interstitial sites and unstrained Si-Si bonds are far more abundant (both $>10^{22}$ cm^{-3}) and are likely to provide ample shallow trapping states for hydrogen, as indicated by the activated diffusion in single-crystal silicon [67,68]. Our model, given by Equations (4-7), implicitly assumes that shallow trapping events not leading to defect absorption occur on time-scales much faster than the formation of defect complexes, so that the diffusion coefficient D_H can be considered constant as a function of time. This is justified by the large number of potential non-defect related trapping sites, which will lead to a fast equilibrium between mobile H and the dominant shallow traps when the flux is turned on. Further supporting this is the high diffusion coefficient of mobile H ($D_H = 3.6^{+0.5}_{-2.3} \cdot 10^{-11}$ cm^{2}s^{-1}) derived from our data: a penetration depth for mobile atomic H of ~ 3 nm (Figure 7) is achieved within 3 ms after the flux is turned on, while the time-scale for defect complexes to equilibrate with the mobile H density is several seconds. Note that the diffusion coefficient D_H strongly affects the H-induced defect profile N_C as a function of depth and time so that it can be obtained from the data with reasonable accuracy, despite the time resolution of only 33 ms.

An important advantage of determining the diffusion coefficient of atomic H from EW-CRDS data over SIMS analysis of atomic deuterium treated a-Si:H films is that the latter is only sensitive to deep trapping events (*i.e.* the exchange of bonded Si-H with Si-D). As pointed out by Kemp *et al.*, capture of D by direct exchange with bonded H is the dominant trapping mechanism in a-Si:H [71]. A front of atomic D moving into the a-Si:H film can therefore be turned into atomic H after the first few monolayers by the efficient exchange at the numerous Si-H sites, which will limit the observed diffusion coefficient

23

of D from the gas-phase. Our experiment is not directly sensitive to these exchange events, only to the trapping of H at a minority of relatively shallow trapping sites and therefore provides a more accurate lower limit on the H diffusion coefficient. The diffusion coefficient of $3.6^{+0.5}_{-2.3} \cdot 10^{-11}$ cm^{2}s^{-1} is similar to that inferred by Das *et al.* from ESR data ($\sim 10^{-10}$ cm^{2}s^{-1}) [35] and approaches the value obtained for c-Si by Van Wieringen and Warmoltz, as well as Seager and Anderson ($\sim 10^{-8}$ cm^{2}s^{-1}, extrapolated to 120 °C) [67,72]. The value we obtain for mobile H diffusion in a-Si:H is sufficiently high to fulfill an important parameter in Branz's H collision model [73,74].

The inserted H density during the steady-state (Figure 7) decays to 1/10 of its value at the surface within $\sim$ 15 nm. The penetration depth for H induced defect creation in a-Si:H determined by Das *et al.* using ESR was on the order of 100 nm [35]. SE studies by Kail *et al.* and Fontcuberta i Morral *et al.* showed that a 25 nm hydrogen-rich subsurface layer is formed during hydrogen plasma-etching of an a-Si:H film [6,69,75], further indicating that a wide range of penetration depths for H from an external source is observed. This difference in penetration depth may also be attributable to the use of plasma in these cases, where energetic H ion bombardment could be argued to lead to greater penetration depths than would be achievable with the neutral (low-energy) hydrogen flux used in this work. Similar to Das *et al.* [35], the penetration depth δ_C for defect formation can be described by:

$$\delta_C \approx \sqrt{\frac{D_H}{k_{ins} N_S}} \qquad (9)$$

Both diffusion coefficient D_H and strained bond density N_S can be expected to easily vary an order of magnitude depending on a-Si:H microstructure; a wide range of penetration depths is therefore likely. Equation (9) only holds for high H fluxes ($\Phi_H > 10^{16}$ cm^{-2}s^{-1}), in the limit of $k_{rec}N_H >> 1/\tau$, where the recombination process dominates the desorption process. At the low fluxes employed in our experiments, the limit $k_{rec}N_H << 1/\tau$ applies and the penetration depth (defined as 10% of induced defect density at the surface) is approximately given by:

$$\delta_C \approx 4\left(\frac{D_H{}^2}{\tau f \Phi_H k_{ins} N_S k_{rec}}\right)^{\frac{1}{3}} \tag{10}$$

The decay of induced defects with depth is not exponential in this case, but follows a z^{-2} dependence. The flux dependence gives a variation of penetration depth between 7 - 11 nm for $\Phi_H = 0.42 \cdot 10^{14}$ cm^{-2}s^{-1} and $2 \cdot 10^{14}$ cm^{-2}s^{-1}, respectively, but this does not significantly affect the observed steady-state s/p ratio as most of the defect absorption occurs in the first 5 nm from the surface, irrespective of flux.

In as-grown material the mobile H density was estimated by Branz to be on the order of 10^{10} cm^{-3} (210 °C) or 10^1 cm^{-3} (25 °C) [76], which is well below the limit of $k_{rec}N_H << 1/\tau$ for the desorption process to dominate the recombination process. Taking this loss process into account is therefore only relevant in the quantitative interpretation of experimental results involving the introduction of large quantities of atomic H to a-Si:H films, such as during growth, deuteration and H annealing of a-Si:H films. Sriraman and Valipa et al. determined through molecular dynamics simulations that repeated

insertion of H in strained Si-Si bonds leads to network relaxation and atomic rearrangement processes [77-79]. Recombination events accompanying the insertion reactions may also be relevant to crystallization, as each recombination event releases up to 4.5 eV of energy in the vicinity of the strained Si-Si bond. We do not observe significant structural changes in the film during repeated H dosing cycles, however, which is attributed to the low atomic H fluxes and short dosing times during the EW-CRDS experiments, as well as the significant pre-treatment of the film with

IV. SUMMARY AND CONCLUSIONS

By measuring the sub-gap absorption of HW-CVD grown a-Si:H during low flux H exposure by time resolved, *in-situ* EW-CRDS, the kinetics of sub-surface atomic H was studied at a substrate temperature of 120 °C. The main conclusions of this work are summarized as follows:

(1)   Fully reversible defect creation under H exposure is observed, with no noticeable passivation of pre-existing defects occurring during repeated H dosing. Using the polarization anisotropy of the absorption, a limited penetration depth of no more than ~15 nm is determined. A kinetic model is presented employing a self-healing 'defect complex', likely a Si-H/dangling bond configuration resulting from the insertion of H in a strained Si-Si bond, which accurately describes the EW-CRDS data as a function of H flux. The lifetime of the defect complex determined from the model is 0.25 ± 0.01 s.

(2)   No effect of H dosing was detected on the surface defect density of a-Si:H. This is likely due to first-order reactions being dominant at 120 °C, which

combined with a fast passivation mechanism, leads to negligible perturbation of the surface H coverage upon H irradiation. However, the possibility of a low absorption cross section for surface defects at the measured wavelength cannot be excluded.

(3)   Based on the t^{-1} dependence of the absorption decay after the H flux is turned off, as well as the finite depth for defect creation and saturation of the defect density at increased H fluxes, a second order process takes place whereby the defect complex acts as a recombination center for the production of H_2, consequently reducing the density of mobile H significantly within 20 nm below the surface. The recombination rate constant $k_{rec} = 10^{+1}_{-6} \cdot 10^{-16}$ cm^{3}s^{-1} is very low, however, so that recombination will only play a significant part in atomic H kinetics at increased mobile H densities occuring during growth, deuteration and H annealing. It should be emphasized, however, that the defects considered here involve a neutral atomic H flux, while the effect of H ions present during plasma processing remains unknown.

(4)   A high diffusion coefficient of $3.6^{+0.5}_{-2.3} \cdot 10^{-11}$ cm^{2}s^{-1} for mobile atomic H is derived from the model, similar to that found by Das *et al.* [35] and close to the value obtained for c-Si by Van Wieringen and Warmoltz, as well as Seager and Anderson [67,72]. This demonstrates that atomic H can penetrate quickly into a-Si:H from an external source, in the absence of deep trapping sites, although the penetration depth is limited to a few tens of nanometers due to recombination. This can be observed in the EW-CRDS experiment, where a 1/10 penetration depth for defects of 15 nm is achieved after 15 s, leading to an effective diffusion

coefficient on the order of 10^{-13} cm^{2}s^{-1}. By separating the contributions of mobile H and trapped H in our model, the underlying kinetics of atomic H transport could be obtained for the case of neutral H on a pre-treated a-Si:H film.

References:

1. R. A. Street, Hydrogenated Amorphous Silicon, Cambridge University Press, Cambridge, United Kingdom (1991).

2. D. L. Staebler and C. R. Wronski, Applied Physics Letters 31, 292 (1977).

3. G. Dingemans et al., Applied Physics Letters 93, 111914 (2008).

4. I. Kaiser, N. H. Nickel, W. Fuhs, and W. Pilz, Physical Review B 58, R1718-R1721 (1998).

5. N. Layadi, P. R. I. Cabarrocas, B. Drevillon, and I. Solomon, Physical Review B 52, 5136 (1995).

6. A. F. i Morral and P. R. i Cabarrocas, European Physical Journal-Applied Physics 35, 165 (2006).

7. K. Saitoh et al., Applied Physics Letters 71, 3403 (1997).

8. H. M. Branz, Solid State Communications 105, 387 (1998).

9. K. Morigaki and H. Hikita, Physical Review B 76, (2007).

10. S. Zafar and E. A. Schiff, Physical Review B 40, 5235 (1989).

11. A. H. M. Smets, C. Wronski, M. Zeman and M. C. M. van de Sanden, Materials Research Society Proceedings 1245, A14.02 (2010).

12. J. Melskens, M. Schouten, R. Santbergen, M. Fischer, R. Vasudevan, D. J. van der Vlies, R. J. V. Quax, S. G. M. Heirman, K. Jäger, V. Demontis, M. Zeman, and A. H.M. Smets, Solar Energy Materials and Solar Cells, 129, 70 (2014).

13. C. R. Wronski and X. Niu, IEEE Journal of Photovoltaics 4, 778 (2014).

14.   J. Melskens, M. Schouten, A. Mannheim, A. S. Vullers, Y. Mohammadian, S. W. H. Eijt, H. Schut, T. Matsui, M. Zeman, and A. H. M. Smets, IEEE Journal of Photovoltaics 4, 1331 (2014).

15.   J. J. Boland, Advances in Physics 42, 129 (1993).

16.   A. Dinger, C. Lutterloh, and J. Kuppers, Chemical Physics Letters 311, 202 (1999).

17.   M. C. Flowers, N. B. H. Jonathan, A. Morris, and S. Wright, Surface Science 396, 227 (1998).

18.   P. Gupta, V. L. Colvin, and S. M. George, Physical Review B 37, 8234 (1988).

19.   W. Widdra et al., Physical Review Letters 74, 2074 (1995).

20.   S. Inanaga, F. Rahman, F. Khanom, and A. Namiki, Journal of Vacuum Science & Technology A 23, 1471 (2005).

21.   Y. Wu et al., Physical Review Letters 77, 2049 (1996).

22.   W. Beyer, Physica B 170, 105 (1991).

23.   I. An, Y. M. Li, C. R. Wronski, and R. W. Collins, Physical Review B 48, 4464 (1993).

24.   R. W. Collins et al., Thin Solid Films 364, 129 (2000).

25.   H. Fujiwara, M. Kondo, and A. Matsuda, Physical Review B 63, art-115306 (2001).

26.   A. A. Langford et al., Physical Review B 45, 13367 (1992).

27.   A. H. M. Smets, W. M. M. Kessels, and M. C. M. van de Sanden, Applied Physics Letters 82, 1547 (2003).

28. B. Abeles, L. Yang, D. Leta, and C. Majkrzak, Journal of Non-Crystalline Solids 97-8, 353 (1987).

29. W. Beyer, Physica Status Solidi A-Applications and Materials Science 159, 53 (1997).

30. W. B. Jackson and C. C. Tsai, Physical Review B 45, 6564 (1992).

31. M. Nakamura and Y. Misawa, Journal of Applied Physics 68, 1005 (1990).

32. P. V. Santos and W. B. Jackson, Physical Review B 46, 4595 (1992).

33. A. E. Widmer, R. Fehlmann, and C. W. Magee, Journal of Non-Crystalline Solids 54, 199 (1983).

34. U. K. Das, T. Yasuda, and S. Yamasaki, Physical Review Letters 85, 2324 (2000).

35. U. K. Das, T. Yasuda, and S. Yamasaki, Physical Review B 63, (2001).

36. S. Yamasaki, U. K. Das, and K. Ishikawa, Thin Solid Films 407, 139 (2002).

37. I. M. P. Aarts et al., Applied Physics Letters 84, 3079 (2004).

38. I. M. P. Aarts, A. C. R. Pipino, M. C. M. V. de Sanden, and W. M. M. Kessels, Applied Physics Letters 90, (2007).

39. W. B. Jackson, D. K. Biegelsen, R. J. Nemanich, and J. C. Knights, Applied Physics Letters 42, 105 (1983).

40. A. H. M. Smets, J. H. van Helden, and M. C. M. van de Sanden, Journal of Non-Crystalline Solids 299, 610 (2002).

41. A. C. R. Pipino, Applied Optics 39, 1449 (2000).

42. I. M. P. Aarts et al., Physical Review Letters 95, (2005).

43. K. G. Tschersich and V. von Bonin, Journal of Applied Physics 84, 4065 (1998).

44. K. G. Tschersich, Journal of Applied Physics 87, 2565 (2000).

45.   Y. J. Chabal and C. K. Patel, Physica 126B, 461-462 (1984).

46.   J. P. M. Hoefnagels, PhD thesis, Eindhoven University of Technology (2005).

47.   P. J. van den Oever, J. J. H. Gielis, M. C. M. V. de Sanden, and W. M. M. Kessels, Thin Solid Films 516, 511 (2008).

48.   A. Gallagher, Thin Solid Films 395, 25 (2001).

49.   E. C. Molenbroek, A. H. Mahan, and A. Gallagher, Journal of Applied Physics 82, 1909 (1997).

50.   W. Zheng and A. Gallagher, Thin Solid Films 501, 21 (2006).

51.   A. H. M. Smets and M. C. M. van de Sanden, Physical Review B 76, (2007).

52.   K. Ohta and H. Ishida, Applied Optics 29, 1952 (1990).

53.   N. Wyrsch, F. Finger, T. J. Mcmahon, and M. Vanecek, Journal of Non-Crystalline Solids 137, 347 (1991).

54.   P. Kisliuk, Journal of Physics and Chemistry of Solids 3, 95 (1957).

55.   A. von Keudell and J. R. Abelson, Applied Physics Letters 71, 3832 (1997).

56.   A. von Keudell and J. R. Abelson, Journal of Applied Physics 84, 489 (1998).

57.   A. von Keudell and J. R. Abelson, Physical Review B 59, 5791 (1999).

58.   C. G. Van de Walle and R. A. Street, Physical Review B 51, 10615 (1995).

59.   R. Darwich, P. Roca I Cabarrocas, S. Vallon, R. Osikovski, P. Morin and K. Zellama, Philosophical Magazine B, 72:3, 363-372 (1995).

60.   W.E. Carlos and P. C. Taylor, Physical Review B 25, 2, 1453 (1982).

61.   R. E. Norberg, D. J. Leopold, P. A. Fedders, R. Borzi, P. H. Chan, J. Herberg and N. Tomic, Materials Research Society Proceedings 609, A26.2 (2000).

62.   U. Hansen and P. Vogl, Physical Review B 57, 13295 (1998).

63. W. Beyer and U. Zastrow, Journal of Non-Crystalline Solids 266, 206 (2000).

64. W. Beyer, Solar Energy Materials and Solar Cells 78, 235 (2003).

65. J. Biener et al., Journal of Vacuum Science & Technology A 21, 831 (2003).

66. H. M. Branz, S. Asher, B. P. Nelson, and M. Kemp, Journal of Non-Crystalline Solids 166, 269 (1993).

67. A. Van Wieringen and N. Warmoltz, Physica 22, 849 (1956).

68. C. G. Van de Walle, P. J. H. Denteneer, Y. Baryam, and S. T. Pantelides, Physical Review B 39, 10791 (1989).

69. F. Kail et al., Philosophical Magazine 84, 595 (2004).

70. N. H. Nickel, W. B. Jackson, and J. Walker, Physical Review B 53, 7750 (1996).

71. M. Kemp and H. M. Branz, Physical Review B 52, 13946 (1995).

72. C. H. Seager and R. A. Anderson, Applied Physics Letters 53, 1181 (1988).

73. Private communication

74. H. M. Branz, Physical Review B 59, 5498 (1999).

75. A. F. I. Morral, J. Bertomeu, and P. R. I. Cabarrocas, Materials Science and Engineering B-Solid State Materials for Advanced Technology 69, 559 (2000).

76. H. M. Branz, Physical Review B 60, 7725 (1999).

77. S. Sriraman, S. Agarwal, E. S. Aydil, and D. Maroudas, Nature 418, 62 (2002).

78. S. Sriraman, M. S. Valipa, E. S. Aydil, and D. Maroudas, Journal of Applied Physics 100, (2006).

79. M. S. Valipa, S. Sriraman, E. S. Aydil, and D. Maroudas, Journal of Applied Physics 100, (2006).
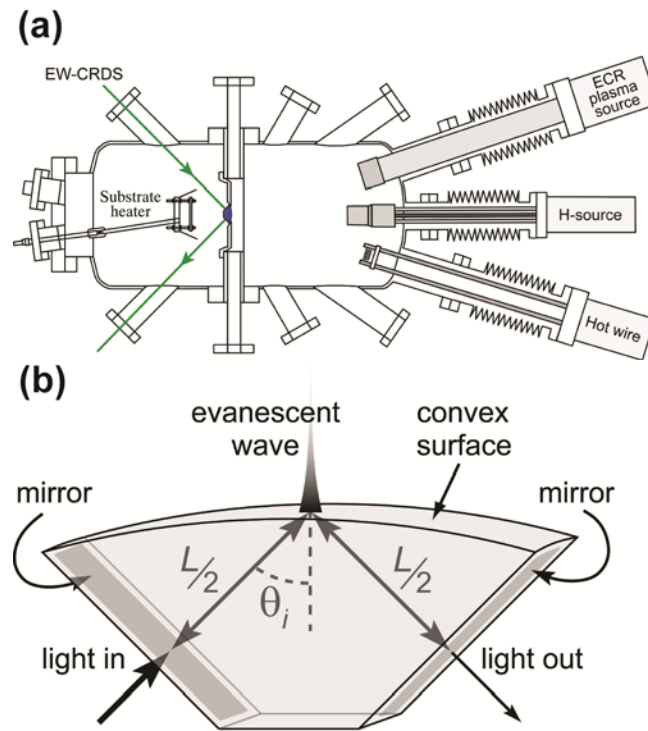
Figures:

Figure 1: (a) The UHV setup with folded cavity as substrate. (b) The monolithic folded resonator showing the two planar, high reflectivity coated (> 99.998%) dielectric mirrors, which is used to detect changes in the sub-gap absorption at 1200 nm of a 42 ± 2 nm a-Si:H film on the convex TIR surface during atomic H dosing.
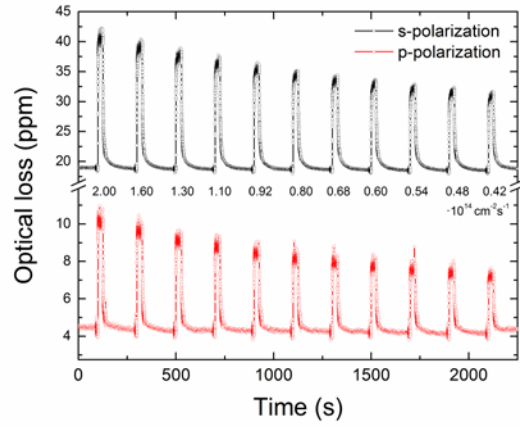
Figure 2: Sub-gap optical loss as a function of time obtained by EW-CRDS during consecutive 30 s H doses with fluxes in the range of $(2\text{-}0.42)\cdot 10^{14}$ $cm^{-2}s^{-1}$ at a substrate temperature of 120 °C. The optical loss of the resonator without thin film was subtracted for both polarizations. The remaining background loss is consistent with a $2.4\cdot 10^{17}$ cm^{-3} bulk defect density.
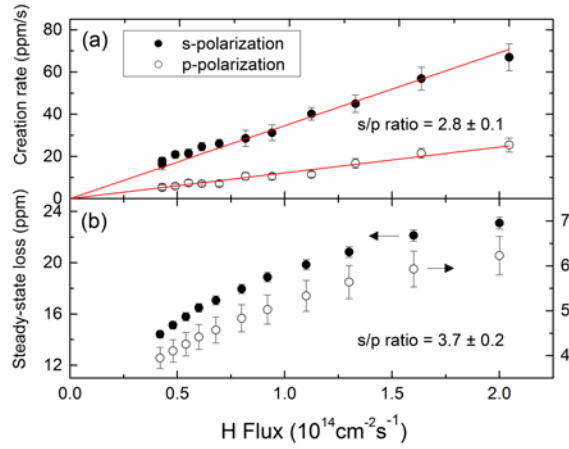
Figure 3: (a) Initial creation rate for both polarizations when the flux is turned on. Each data point is the result of an exponential fit during the first second after the hydrogen dosing is started. Error weighted linear fits reveal an initial s/p ratio of 2.8 ± 0.1. (b) Steady-state optical loss as a function of flux. The steady-state s/p ratio as a function of flux is constant within the measurement error with a value of 3.7 ± 0.2.
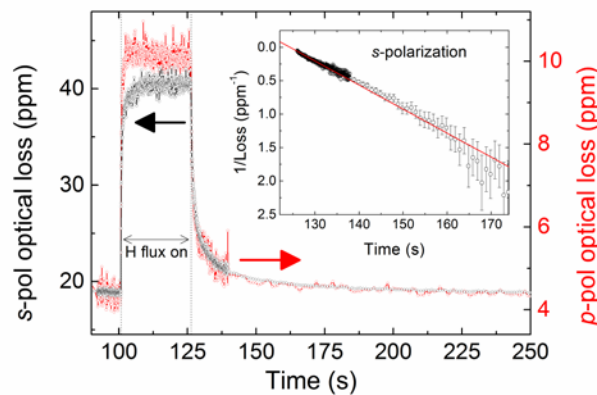

Figure 4: A single dosing cycle at an H flux of $2.00 \cdot 10^{14}$ cm^{-2}s^{-1}, clearly showing the polarization anisotropy as a function of time. The inset depicts the inverse of the s-polarized decay after the H flux is terminated along with a linear fit, revealing its hyperbolic character.
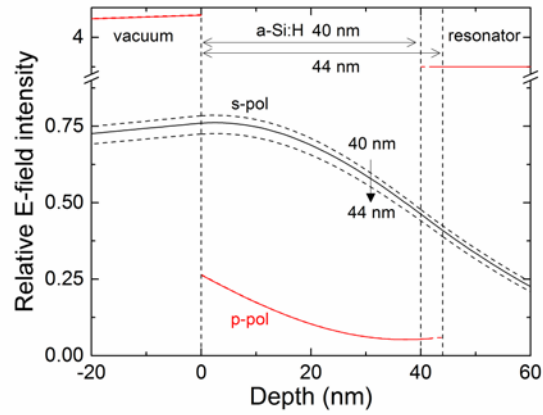
36

Figure 5: Calculated s- and p-polarization relative E-fields at 1200 nm using refractive indices of 1.49, 3.60 and 1.00 for the resonator, 42 ± 2 nm a-Si:H thin film and vacuum, respectively. The plane-wave has an angle of incidence of 45° at the resonator-thin film interface and is at an angle of 16.5° within the a-Si:H film. An evanescent field is formed in the vacuum. The p-polarization E-field has a negligible sensitivity to the film thickness.
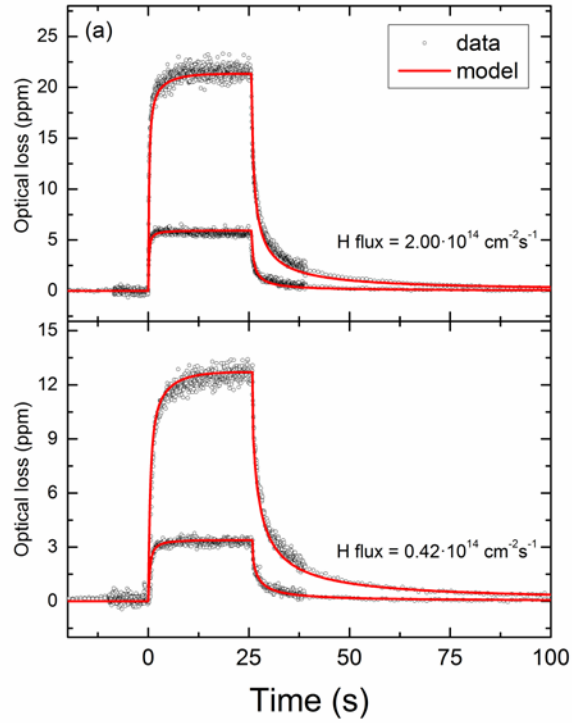
Figure 6: Model fits to the data with $k_{ins}N_S = 800$ s^{-1}, $k_{rec} = 10^{-15}$ cm^{3}s^{-1}, $\tau = 0.25$ s, $D_H = 3.6 \cdot 10^{-11}$ cm^{2}s^{-1} and $f = 5.5 \cdot 10^{-3}$, (a) the highest and lowest flux data and model as a function of time with background loss subtracted for both polarization directions, (b) steady-state induced loss, initial creation/healing rate when the flux is turned on/off as a function of H flux compared to the model prediction.
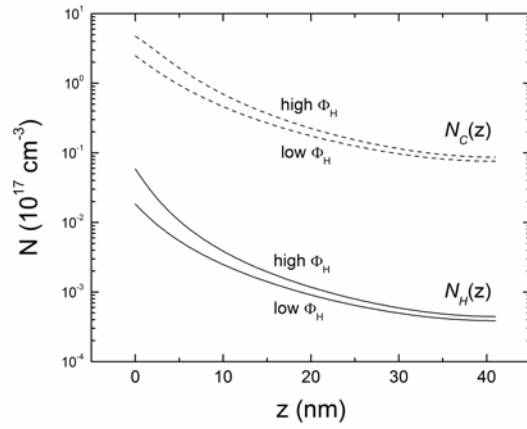
Figure 7: Calculated defect complex (N_C) and mobile H (N_H) profiles as a function of depth for the highest and lowest H fluxes ($2.00 \cdot 10^{14}$ and $0.42 \cdot 10^{14}$ cm^{-2}s^{-1}, respectively). The 1/10 penetration depth for the defect complex is ~ 15 nm, opposed to ~ 8 nm for the mobile H density.